Article:
Wang, Z., He, X., Bu, T. et al. (8 more authors) (2024) A Full-Process, Fine-Grained, and Quantitative Rehabilitation Assessment Platform Enabled by On-Skin Sensors and Multi-Task Gait Transformer Model. Advanced Materials, 36 (46). 2408478. ISSN: 0935-9648

https://doi.org/10.1002/adma.202408478

A full-process, fine-grained, and quantitative rehabilitation assessment platform enabled by on-skin sensors and multi-task gait transformer model

Zhixin Wang[1], Xinrun He[2], Tianzhao Bu[1], Bo Pang[1], Wei Guo[1], Zhongyi Tu[3], Zhiqiang Zhang[4], Xiling Xiao[3], Zhouping Yin[1]*, Jian Huang,[2]* Hao Wu[1,5]**

[1]Flexible Electronics Research Center, State Key Laboratory of Intelligent Manufacturing Equipment and Technology, School of Mechanical Science and Engineering, Huazhong University of Science and Technogy, Wuhan 430074, China

[2]Ministry of Education Key Laboratory of Image Processing and Intelligent Control, School of Artificial Intelligence and Automation, Huazhong University of Science and Technology, Wuhan 430074, China

[3]The Department of Rehabilitation Medicine, Union Hospital, Tongji Medical College, Huazhong University of Science and Technology, Wuhan 430022, China

[4]School of Electronic and Electrical Engineering, University of Leeds, LS2 9JT, Leeds, U.K.

[5]School of Integrated Circuits, Huazhong University of Science and Technology, Wuhan, China

Z.X.W. and X.R.H. contributed equally to this work.

*Corresponding author. Email: Xiaoxiling23@126.com; yinzhp@hust.edu.cn; huang_jan@mail.hust.edu.cn; hwu16@hust.edu.cn

Keywords: on-skin sensors, MG-former model, full-process rehabilitation assessments, lower limb movement disorders

Abstract

Rehabilitation of patients with lower limb movement disorders is a gradual process, which requires full-process assessments to guide the implementation of rehabilitation plans. However, the current methods can only complete the assessment in one stage and lack objective and quantitative assessment strategies. Here, we develop a full-process, fine-grained, and quantitative rehabilitation assessments platform (RAP) supported by on-skin sensors and a multi-task gait transformer (MG-former) model for patients with lower limb movement disorders. The signal quality and sensitivity of on-skin sensor is improved by the synthesis of high-performance triboelectric material and structure design. The MG-former model can simultaneously perform multiple tasks including binary classification, multiclassification, and regression, corresponding to assessment of fall risk, walking ability, and rehabilitation progress, covering the whole rehabilitation cycle. The RAP can assess the walking ability of 23 hemiplegic patients, which has highly consistent results with the scores by the experienced physician. Furthermore, the MG-former model outputs fine-grained assessment results when performing regression task to track slight progress of patients that cannot be captured by conventional scales, facilitating adjustment of rehabilitation plans. This work provides an objective and quantitative platform, which is instructive for physicians and patients to implement effective strategy throughout the whole rehabilitation process.

1. Introduction

Many diseases such as stroke, Parkinson's disease, hemophiliac arthritis, etc., affect the human body in the form of abnormal gait, resulting in the rising prevalence of lower limb movement disorders, which cause great inconvenience or even life-threat to the large number of patients[1]. For instance, there are about 10 million new cases of stroke alone every year in the world, of which more than 70% of patients suffer from movement disorders. Modern medical theory and clinical medicine have proved that apart from early surgical and pharmacological treatment, scientific rehabilitation training is equally important for patients with lower limb movement disorders[2]. In particular, gait analysis and walking ability assessment are critical components in rehabilitation medicine that allow physicians to assess ambulatory ability, diagnose diseases, and formulate personalized rehabilitation programs[3]. However, conventional gait analysis and walking ability assessment depend on the observation of physicians regarding patients' movement, resulting in subjective results, while assessments based on conventional scales lack fine-grained results[4]. For example, the conventional Brunnstrom scale consists of only six levels, and the Tinetti gait assessment scale can only give integer values within 0-12 points, which is difficult to capture the slight progress made by patients in rehabilitation[5]. Besides, the assessment process is usually carried out manually by physicians, which is difficult to meet the growing needs of rehabilitation due to the workload burden[6].

The rapid development of sensing technology has rendered gait analysis and rehabilitation assessments more convincing with the support of quantitative data, which provides a new assessment approach for clinicians to formulate more refined training programs[7]. Among them, vision-based motion capture systems acquire spatial-temporal parameters during walking, which can provide comprehensive information

about human movement[8]. Nonetheless, the motion capture systems are usually complex and expensive, requiring skilled operators, and the recognition results can be significantly affected by camera position and ambient light intensity[5a]. In terms of wearable devices, inertial measurement units (IMUs) or pressure sensors are widely adopted solutions to obtain information of human gait[9]. However, the gait monitoring devices equipped with IMUs are bulky and inflexible, causing not only discomfort but also errors in velocity and position data due to noise and signal drifting, while utilizing plantar pressure distribution information alone is inadequate for those who require more detailed gait information[10]. Besides, the surface electromyography (sEMG) combined with kinematic and kinetic data is an effective approach to further assess muscle activity levels and gait coordination[11]. Nevertheless, the weak sEMG signal strength (in microvolts) and low signal-to-noise ratio affect the accuracy of assessment[12]. A potential solution to address the above challenges lies in triboelectric sensors, which are widely used to sense human motion and physiological activities by the high-quality electric signals[11b, 13]. Fundamentally, the surface charge density induced by the difference in electron affinity between two triboelectric materials greatly determines the performance of triboelectric sensors[14]. Therefore, synthesis and optimization of triboelectric materials are essential to achieve high electron affinity differences to enhance the output performance of triboelectric sensors[15].

Artificial intelligence technology has been widely adopted for disease diagnosis and rehabilitation assessments, which has greatly promoted major progress in the field and provided more reliable yet simpler solutions to complicated tasks. Previous studies have utilized multi-feature fusion methods or support vector machines (SVM) by integrating dynamic and physiological data to distinguish different walking patterns in stroke patients. However, the multi-feature fusion and SVM require prior feature selection and

99 extraction, which may be suboptimal for time-series data, such as complex gait
100 signals[16]. Although deep learning approaches including convolutional neural networks
101 (CNN) and long short-term memory (LSTM) can automatically learn gait features, the
102 quantitative assessment of patients' walking ability cannot be achieved [17]. Besides, the
103 current algorithmic models can only perform a single-task in one stage of rehabilitation,
104 which hardly meets the needs of full-process rehabilitation assessments[18]. Hence, a
105 full-process and fine-grained rehabilitation assessments platform to quantitatively
106 assess the walking ability of patients is still highly desired.

107 In this work, we develop cost-effective on-skin sensors and an MG-former model to
108 build a full-process, fine-grained, and quantitative RAP for patients with lower limb
109 movement disorders. The on-skin sensors based on the coupling effect of contact
110 electrification and electrostatic induction are attached on the surface of dominant
111 muscle/tendon groups in lower limb to detect the deformation of skin during dynamic
112 gait movements and generate a series of electric signals. In addition, the signal quality
113 of the on-skin sensor is improved by synthesized triboelectric material and structure
114 design, with an average peak amplitude approximately 470 times higher than that of
115 traditional biopotential electromyography methods, demonstrating a promising method
116 for diagnosis and rehabilitation assessments. Based on the tasks of binary classification,
117 multiclassification, and regression performed by the MG-former model, the RAP can
118 complete the fall risk assessment, walking ability assessment, and rehabilitation
119 progress assessment, which covers the whole rehabilitation cycle and realizes full-
120 process rehabilitation assessments (Stage 1-3 in **Figure 1**a). By means of continual
121 learning, the MG-former model achieves an iterative update that improves the
122 assessment accuracy of the RAP from 90.67% to 93.33%. Besides, the results of the
123 RAP-based assessment of 23 hemiplegic patients match the scores obtained by

experienced physician according to the conventional Tinetti gait assessment scale. Furthermore, the rehabilitation progress assessment of patients with lower limb movement disorders for three consecutive weeks is completed to capture the slight progress based on the regression prediction task of the MG-former model, which is instructive for enhancing the patients' motivation and adjusting the rehabilitation plans.

2. Results

2.1 Overview of the RAP and working principle

Figure 1a serves as a proof-of-concept demonstration of the full-process, fine-grained, and quantitative RAP based on on-skin sensors for gait diagnosis and rehabilitation assessments of patients with lower limb movement disorders, including fall risk assessment (Stage 1), walking ability assessment (Stage 2), and rehabilitation progress assessment (Stage 3), respectively. The flexible on-skin sensors are positioned on key muscle groups in the lower limb, which monitor overall movement patterns and behaviors of the patients, providing valuable data for gait diagnosis and rehabilitation assessments. The RAP integrates time-frequency domain analysis and MG-former model to perform multiple tasks such as binary classification (Task 1), multiclassification (Task 2), and regression (Task 3), corresponding to fall risk assessment, walking ability assessment, and rehabilitation progress assessment, respectively (Figure 1d). Here, a pair of high-elasticity triboelectric materials (polydimethylsiloxane/$CaCu_3Ti4O_{12}$ nanoparticles (PDMS/CCTO) composite film and electrically conductive composites (ECC)) were developed to ensure the sensor can be conformally attached to detect subtle deformation resulting from lower limb movement during gait monitoring and rehabilitation assessments. Figure 1b presents a schematic diagram of the on-skin sensor, which consists of upper and lower layers. The upper

layer is formed by a PDMS encapsulation layer, a PDMS/CCTO composite triboelectric layer, and a silver nanowires (AgNWs)-based top electrode. The uppermost PDMS film can be used as an encapsulation layer to protect AgNWs, which can reduce the interference of charges carried on external objects and improve the sensing accuracy. Figure S2a illustrates the scanning electron microscopy (SEM) image of AgNWs, which clearly shows that the single AgNW with a diameter of about 60 μm and the AgNWs are interspersed with each other to form a conductive network, improving the ductility of electrodes. The lower layer of on-skin sensor consists of ECC as bottom electrode and triboelectric layer, and a PDMS substrate with arc-shaped protrusions arranged in a circumferential array[19]. Notably, the arc-shaped protrusions were utilized as the support structure for better separation after contact between the two triboelectric layers.

Figure S2b shows the cross-sectional diagram of the ECC, where the thicknesses of PDMS substrate and ECC electrode are about 220 μm and 50 μm, respectively, which facilitates the conformal adhesion of on-skin sensor to skin surface to effectively perceive the deformation of muscle/tendon. Besides, the side contacted with PDMS/CCTO composite film presents a rough surface (Figure S2c), which increases the effective contact area of the triboelectric layers, improving the signal quality. Both the materials of the triboelectric pair in our study are highly stretchable and flexible (maximum tensile limit of about 100%), enabling the accurate monitoring of skin deformation (Figure S2d and e). More importantly, the ECC can be prepared with the same polymer as the substrate, such as PDMS, to ensure strong adhesion between interconnects and the substrate. Figure 1c-i and c-ii display the front and side optical images of the on-skin sensor, respectively, and the specific fabrication details are displayed in Section 4 and Figure S1a and b. Figure S2f-h show the on-skin sensor

174 during various mechanical deformation such as stretching, twisting, and bending,
175 demonstrating its good flexibility. Notably, all of the materials for building the key
176 components of the on-skin sensor are low-cost and fabricated through inherently
177 scalable and cost-effective methods. The fabricated on-skin sensor can actively capture
178 somatosensory signals by muscle motion (flexion and extension) and convert them into
179 distinguishable electric signals based on the coupling of triboelectrification and
180 electrostatic induction effect. The detailed working principle is elaborated in Figure S3
181 and Note S1, Supporting Information.

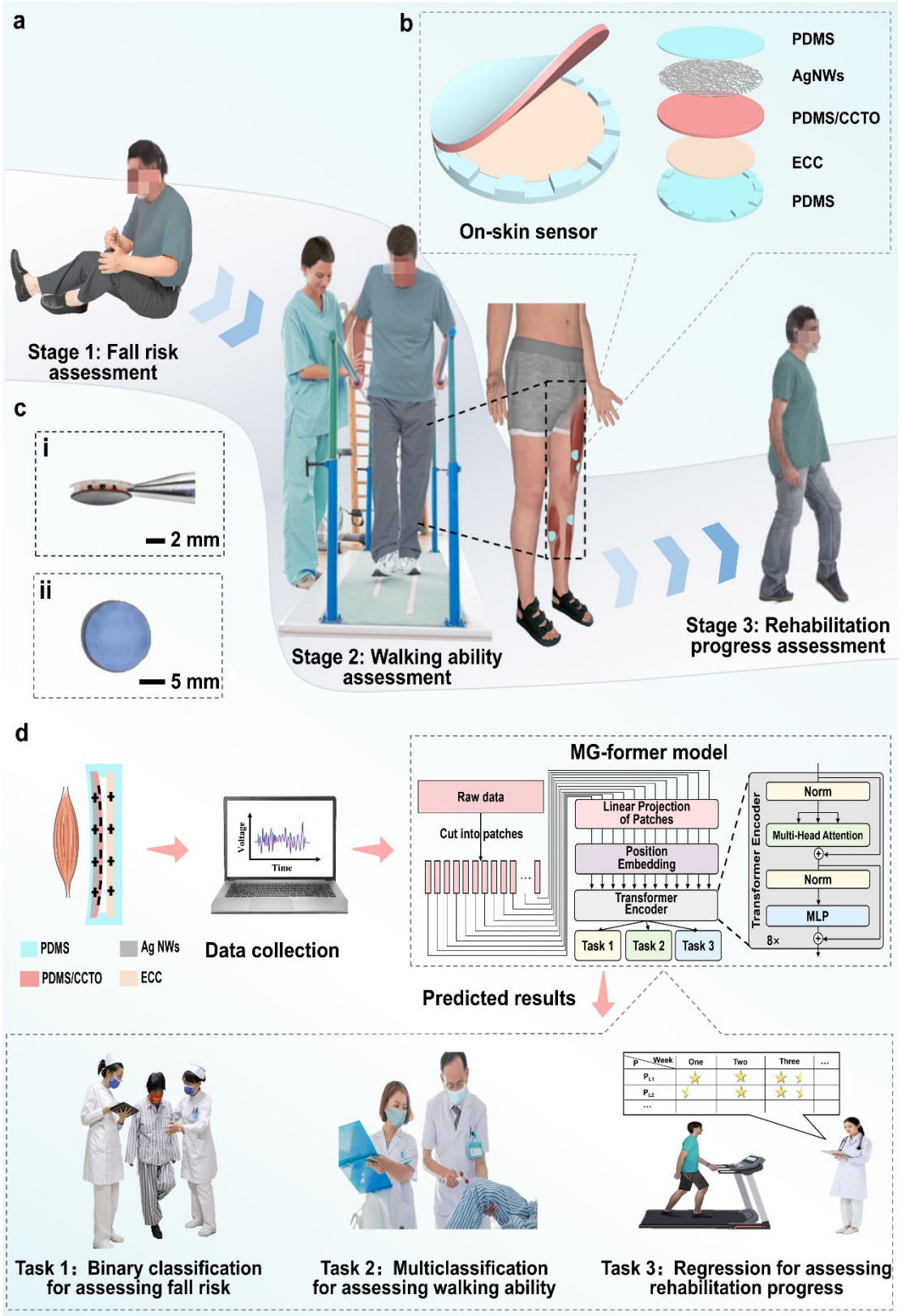

Figure 1. Schematic illustration of the RAP. a) The proof-of-concept demonstration of the full-process rehabilitation assessments platform. b) Schematic diagram of the on-skin sensor. c-i and c-ii) The front and side optical images of the on-skin sensor. d) Schematic diagram of the full-process rehabilitation assessments for patients with lower limb movement disorders based on MG-former model.

2.2 Performance optimizations and characterizations of the on-skin sensor

Typically, the output of the triboelectric sensor is inextricably related to the surface charge density of the triboelectric material[15]. The maximum surface charge density (σ) is proportional to ε_r/d ($\sigma \propto \frac{\varepsilon_r}{d}$), where ε_r and d are the relative dielectric constant and effective dielectric thickness of the triboelectric layer[20]. Based on literature review results (Table S10)[15, 21], CCTO with a significantly higher dielectric constant (ε_r = 7500) was selected as the dopant to improve the performance of the on-skin sensor. The CCTO is typical cubic-shape nanocrystal with an average particle size of ~300 nm, which are demonstrated by the SEM, transmission electron microscopy (TEM) and X-ray Diffraction (XRD) results (**Figure 2**a-c)[21e]. The inset of Figure 2a shows that elemental mapping was performed by energy dispersive spectroscopy (EDS) measurement to confirm the distribution of Ti, O, Cu, and Ca. Figure 2d shows the ε_r of composite films with different weight percentages (wt%) of CCTO. The results indicate that the addition of CCTO can significantly improve the ε_r of the PDMS/CCTO composite film. Specifically, compared to pure PDMS, the ε_r of PDMS/CCTO composite film is greatly enhanced from 4.7 (0wt% CCTO) to 8 (20wt% CCTO) at a frequency of 1k Hz. The incorporation of high dielectric constant materials, such as CCTO, into the base material (PDMS) enhances the dielectric constant by strengthening the polarization effect. This is attributed to the strong electric dipoles and high charge densities in the molecular structure of these materials, which facilitate charge redistribution and rearrangement under an external electric field[15]. The formation of strong polarization interfaces between the high dielectric constant materials and PDMS further enhances the polarization effect, leading to an increase in the dielectric constant

of the composite films. Figure 2f displays the dependence of ε_r on temperatures ranging from 25 ℃ to 125 ℃ at frequency of 1 kHz, where ε_r decreases slightly with increasing temperature, which suggests that the PDMS/CCTO composite films exhibit excellent thermal stability. The surface roughness of the PDMS/CCTO composite films is shown in Figure 2g. It can be observed that the surface roughness of composite films increases with the increase of the content of CCTO. This can be attributed to the fact that as the doping concentration of CCTO increases, some CCTO particles tend to aggregate and cluster on the surface of the PDMS/CCTO composite film, leading to an increase in surface roughness[21d]. The surface potential of the composite films was also examined by Kelvin probe force microscopy (KPFM) to further clarify the relationship between the doping content and the surface potential of the composite films. The contact potential difference (V_{CPD}) between the testing sample and platinum (Au) tip is determined by the equation:[22]

$$V_{CPD} = \frac{\varphi_{tip} - \varphi_{sample}}{-e} \quad (1)$$

where φ_{tip} and φ_{sample} represent the work function of the tip and the sample, respectively, e is electronic charge (1.6×10^{-19} C). Since φ_{tip} is constant, the work function of the sample increases with the decrease of V_{CPD} value. The increase in work function renders the electron energy level lower, leading to easier reception of electrons on the PDMS/CCTO composite films during contact electrification. Figure 2h-i depicts that the V_{CPD} of pure PDMS is only -2.53 V, demonstrating the weak electron reception ability. By gradually adding CCTO powder into PDMS with gradient, the V_{CPD} value of the composite films was changed from -3.04 V (4%) to -5.51 V (20%), leading to a significant improvement in the charge-attracting property (Figure 2h-ii to Figure 2h-vi).

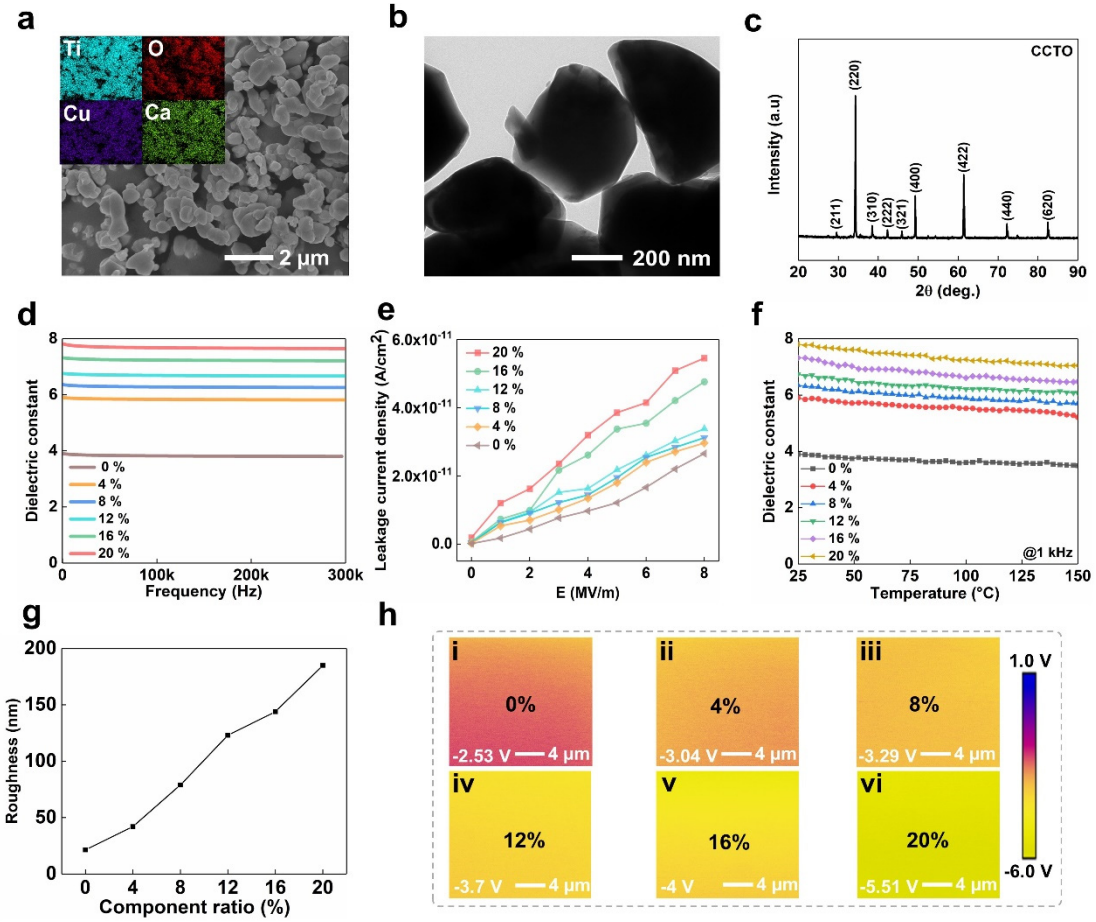

Figure 2. Characterizations and optimizations of the PDMS/CCTO composite films. The a) SEM, b) TEM, and c) XRD of CCTO nanoparticles. d) The ε_r and e) leakage current density of PDMS/CCTO composite films with the CCTO content from 0 to 20 wt%. f) The ε_r as a function of temperature at 1 kHz. g-h) The surface roughness and surface potential of the PDMS/CCTO composite films with different content of CCTO.

To evaluate the effect of CCTO content on the surface charge density of the composite film, the performance of the on-skin sensor made from composite films with different doping ratios were systematically characterized. As can be seen from **Figure 3**a-c, the open circuit voltage (V_{OC}), short circuit current (I_{SC}), and short circuit transfer charge (Q_{SC}) increase initially followed by an obvious decrease from wt% of 0% to 20%. The highest value of the V_{OC}, I_{SC}, and Q_{SC} is 11.4 V, 0.4 μA, and 3.11 nC, respectively, at the doping ratio of 16%. Besides, when the content of CCTO is 0% (i.e., pure PDMS), the V_{OC}, I_{SC}, and Q_{SC} are only 6.99 V, 0.23 μA, and 2.02 nC, which is increased by 64%, 73%, and 53%, respectively, when the wt% reaches 16%. This is due

to the increase of ε_r for composite film to capture charges, which improves the performance of the on-skin sensor. In other words, the more negative the surface potential value of PDMS/CCTO composite films, the more electron receiving ability can be enhanced, which is consistent with the corresponding electrical output characteristics of the electron (Figure 2h). Nevertheless, it is worth noting that the V_{OC}, I_{SC}, and Q_{SC} decreased obviously at a CCTO content of 20%, which is due to the fact that a high content of CCTO leads to a significant increase in the leakage current inside the composite film (Figure 2e), thereby canceling out the triboelectric charges and ultimately decreasing the output performance[20]. In addition, we also further investigated the output performance of the on-skin sensor under different external forces (Figure S5a-c), a linear motor (Figure S6) controlled by computer programming was used to provide different loads and observed that output performance increased gradually with increasing external force from 3.7 V, 0.14 μA, and 1.41 nC at 5 N to 11.4 V, 0.4 μA, and 3.11 nC at 25 N. This is because the increase in the external force increases the effective contact area between the two triboelectric layers, resulting in more charge transfer to enhance the output performance.

Optimizing the performance of the on-skin sensor involves not only analyzing the influence of triboelectric materials, but also considering the structure of the sensor. Here, the shape of the on-skin sensor was designed to be circular because the curvature of the circular boundary is the same, which results in a small and uniform stress distribution[23]. The height of the arc-shaped protrusion (h) and the size of the central angle (α) were chosen as key parameters to further investigate the subtle relationship between the on-skin sensor structure and its performance. Figure 3d shows the stress distribution of on-skin sensors with different α, which were analyzed by finite element analysis. Clearly, the stress is relatively more uniform when α is decreasing at the same applied pressure

(1 N). However, a relatively smaller central angle (10°) results in a smaller area for each arc-shaped protrusion, which leads to poor adhesion with the upper layer and affects the durability of the on-skin sensor. Therefore, 15° is selected as the center angle in this work. This carefully selected angle ensures that the stress distribution remains relatively uniform while maintaining a sufficient area for each arc-shaped protrusion, thereby promoting robust adhesion and durability. The height of the arc-shaped protrusion determines the distance between the two triboelectric layers. Figure 3e describes the influence of the height of the arc-shaped protrusions (0.4, 0.8, and 1.8 mm) on the output signal of the on-skin sensor. Specifically, the on-skin sensor with *h* of 0.8 mm achieved the best sensitivity, reaching 0.79 V/N, higher than the other two sensors in the same force range (0.5-3 N). In addition, the signal obtained by the on-skin sensor was compared with the commercial sEMG electrode to further demonstrate the superiority of the on-skin sensor to retrieve muscle/tendon movement information. Figure 3f shows the placement of an on-skin sensor (position 1) and the commercial sEMG electrodes (position 1-3) on the right lower limb, which demonstrates the convenience of the on-skin sensor. It is evident that the signal of the on-skin sensor (1124 mV) displays more distinctive feature than sEMG signal (2.39 mV) during dorsiflexion of foot movement, with an average peak amplitude approximately 470 times higher than sEMG (Figure 3g). Furthermore, the quality of the on-skin sensor signal exhibits a significantly higher signal-to-noise ratio (SNR) of 34.07 dB in comparison with the sEMG device's SNR of 18.34 dB (Figure 3h). The on-skin sensor's higher sensitivity allows it to capture more subtle signals, but it may also amplify the noise floor, resulting in a smaller difference in SNR compared to sEMG. Therefore, although the average amplitude of the on-skin sensor is much larger than that of the sEMG signal, the SNR of the on-skin sensor is not significantly increased compared

with the sEMG signal due to large signal noise. The more in-depth derivation and calculation can be obtained from Note S2, Supporting Information. Figure 3i depicts that the response and recovery time of on-skin sensor under the same pressure are only 53.6 ms and 64.2 ms, respectively, which further ensure the effective capture of human gait-related triboelectric signals. The performance of the on-skin sensor remains almost constant after about four months (Figure S7a) and 4, 000 cycles under different loading forces (Figure 3j and Figure S7b-f, corresponding to 4 N, 5 N, 10 N, 15 N, 20 N, and 25 N, respectively.), which proves the great stability and reliability of the on-skin sensor as a feasible method for long-term rehabilitation monitoring applications. Besides, Figure S7b and g-i illustrate the relationship between the humidity and the output performance of the on-skin sensor. It is worth noting that although the increase in humidity inhibits the active ability of some of the electrons, resulting in a slight decrease in performance, the output of the on-skin sensor remains relatively stable at 54% humidity.

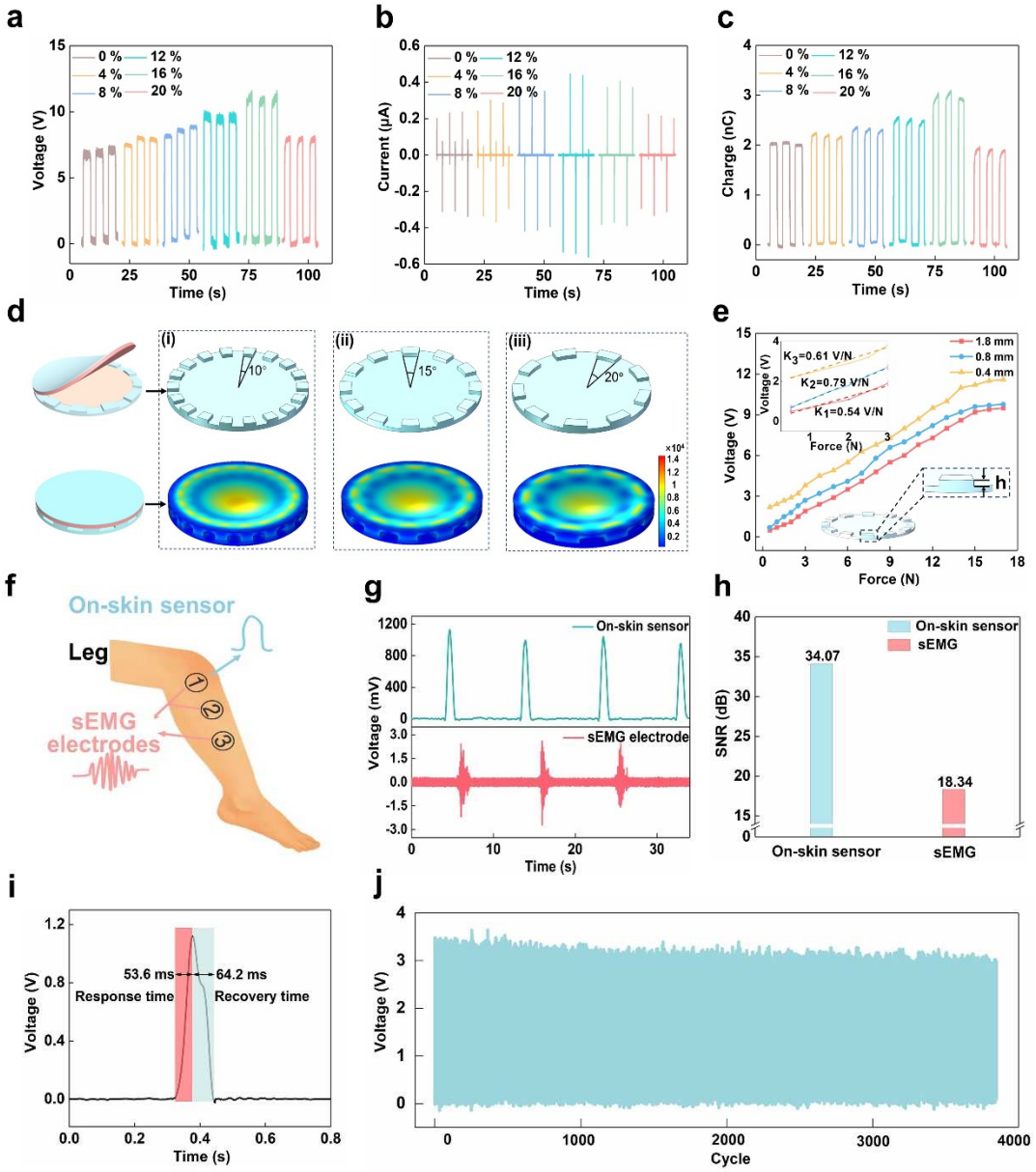

Figure 3. Characterizations and optimizations of the on-skin sensor. a-c) The V_{OC}, I_{SC}, and Q_{SC} of the on-skin sensor with different content of CCTO. d) The stress distribution of the on-skin sensor with different α were analyzed by finite element analysis. e) The influence of the height of the arc-shaped protrusions on the output signal of the on-skin sensor. f) The schematic illustration showing the placement of the on-skin sensor and the commercial sEMG electrodes on the right lower limb. g) The corresponding output voltage signals generated by the on-skin sensor and the sEMG electrodes, respectively. h) The SNR value of the on-skin sensor and sEMG electrodes. i) The response and recovery time of the on-skin sensor. j) The stability testing of the on-skin sensor.

2.3 Diagnosis and symptom analysis of abnormal gait

As one of the most common behavioral characteristics, gait is not only instinctively controlled by human joints, muscles, and nervous system, but also affected by key

information such as biomechanical and kinematic parameters[24]. According to the muscle functions of each part in Table S1, the rectus femoris (RF), vastus lateralis (VL), tibialis anterior (TA), and gastrocnemius (GM) were selected as signal source muscles for diagnosis and rehabilitation assessments (Figure S8)[25]. Figure S9a and b illustrate the optical images of the on-skin sensors on the lower limbs, respectively. The on-skin sensor is firmly adhered to the skin surface by a medical waterproof polyurethane (PU) film[26]. Besides, a pair of force sensing resistors (FSR) labeled FSR1 and FSR2 were arranged on the front and back sides of a shoe to capture plantar pressure signals during walking (Figure S9c).

As depicted in **Figure 4**a and b, the gait phase of one lower limb, which can be divided into stance phase (Pre-stance, Mid-stance, and Ter-stance) and swing phase (Pre-swing and Ter-swing) by plantar pressure signals, where the stance phase is characterized by the stability of body's center of gravity, while the swing phase involves the active forward swing of lower limb[27]. Figure 4b and Figure S10a illustrate the gait signals generated by a healthy subject (H1) walking on a treadmill at regular speed. It can be seen that most of the signals of on-skin sensors generated by muscle triggering occur in swing phase, which is due to the fact that during the swing phase, the human body needs to quickly adjust the posture and orientation as well as maintain the body balance. Specifically, during the stance phase the muscles are in a contracted state causing the two triboelectric layers to contact each other so that no charge transfer occurs (Figure S3i). In contrast, the muscle relaxation during the swing phase causes the two triboelectric layers to separate, generating a variable electric field that drives the flow of free electrons in an external circuit to form a current (Figure S3ii). As can be observed from Figure 4b, the time interval (T) between voltage signal peaks can represent step frequency (1/T), while the signal amplitude reflects the strength of

contraction or propulsion force generated by the muscle. Meanwhile, the duration of stance phase is about 60% of the whole gait cycle, which can also be demonstrated by the experimental results of two other subjects (Figure S10b and c). We further investigated the attachment of the on-skin sensor to the skin and evaluated its stability and potential skin irritation or discomfort during long-term wear. It can be seen that after 2 hours of continuous wear, there is no adverse reaction, irritation or discomfort on the part of the human skin in contact with the sensor or PU film (Figure S10e and f). Besides, the human skin in contact with the sensor can be recovered to the initial state in about 8 minutes (Figure S10h-j), which again demonstrates that the on-skin sensor does not cause irritation or discomfort to the skin even if worn for a long time. Moreover, the upper and lower layers of the on-skin sensor are connected tightly without any delamination (Figure S10g). The stability of the on-skin sensor was demonstrated through long-term testing of the subject wearing the on-skin sensor (*e.g.*, tibialis anterior (TA)), as shown in Figure S10d. The result shows that there is no obvious decay or degradation of the output voltage during gait data collection, which validates good stability and reliability of on-skin sensor.

In general, the impact of many diseases on the human body is exhibited in the form of abnormal gait. For instance, the gait of the patient with post-stroke hemiplegia (Figure 4c) is mostly characterized by instability, poor symmetry, abnormal rhythm, and reduced balance and coordination[6]. Figure 4d and e present the gait signals of two post-stroke hemiplegic patients (P1 and P2, as shown in Figure S11a and b, corresponding to Movie S1 and Movie S2.) during walking at an adaptive speed on a treadmill. As shown in Figure 4f and Movie S1, the peak-to-peak value of the on-skin sensor signal generated by GM muscle deformation ($V_{PP\text{-}GM}$) is the highest in a normal person, followed by the unaffected side of P1, while the affected side of P1 is the lowest.

Notably, the power spectral densities of $V_{PP\text{-}GM}$ also exhibit a similar trend, which can give a key feature to assess the progress made by the patients during rehabilitation. This difference is mainly due to the reduced or even loss of motor ability on the side of body caused by the damage of central nervous system (CNS), while the muscle strength on the unaffected side is relatively stronger, which renders the muscle deformation more pronounced during walking and enhances the amplitude of the triboelectric signals[28]. Besides, as presented in Figure 4d-i and d-ii, the duration of the stance phase on the affected side is slightly shorter than that on the unaffected side ($t_{1U} > t_{1A}$), while the swing phase shows the opposite trend ($t_{2U} < t_{2A}$). This is because hemiplegia has reduced weight-bearing capacity on the affected side, which cannot provide adequate support during walking. In order to maintain the stability of the body, it is necessary to rely on the unaffected side to compensate for part of the weight[6, 29]. Therefore, patients with post-stroke hemiplegic walk with a shorter duration of stance phase and a longer duration of swing phase on the affected side compared to the unaffected side, demonstrating an asymmetry in the spatiotemporal parameters of gait. For P2 (Movie S2), the gait signal on the unaffected side presents the same irregular characteristics as the affected side, which can be reflected by the low amplitude and chaotic oscillatory signals from the sensors (Figure 4e-i and e-ii). This is because the P2 is more severely than P1 and requires orthosis to maintain correct posture and provide stable support in daily life. Clearly, long-term compensation for the loss of muscle function on the affected side also affect the function of the unaffected side.

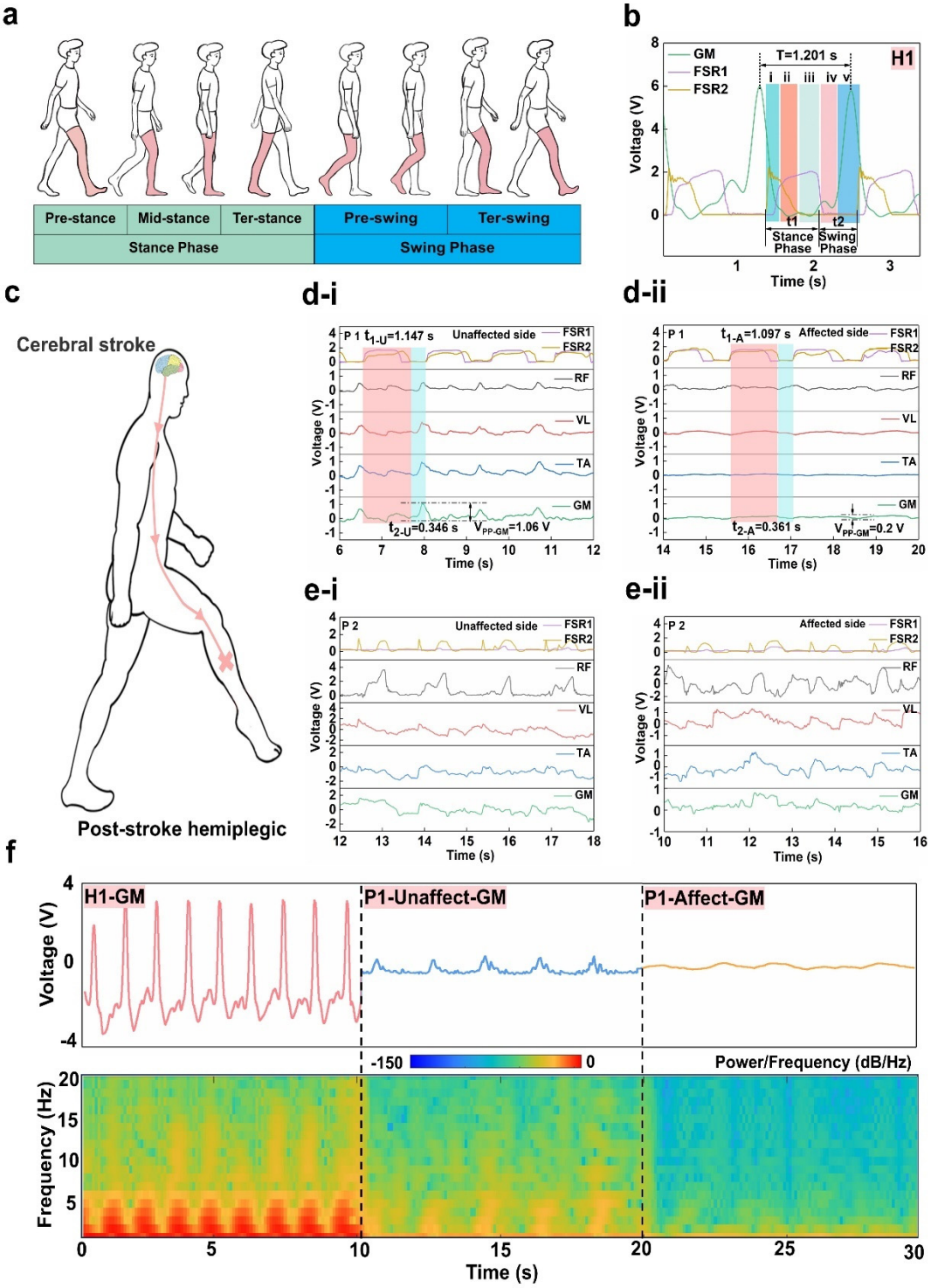

Figure 4. Diagnosis and symptom analysis of patients with post-stroke hemiplegia (P1 and P2). a) Schematics of a typical gait cycle and b) the corresponding signals of normal walking. c) Schematic diagram of walking for a stroke patient with hemiplegia. The gait signals on the unaffected side d-i) and affected side d-ii) of P1. The gait signals on the unaffected side e-i) and the affected side e-ii) of P2. f) The voltage signals (top) generated by the GM of H1, the unaffected side, and affected side of P1, respectively, and their power spectral densities (bottom).

2.4 The full-process rehabilitation assessments platform based on MG-former model

The full-process rehabilitation assessments (Stage1-3: fall risk, walking ability, and rehabilitation progress assessment) are indispensable parts of the rehabilitation process for patients with lower limb movement disorders, which is of great importance in guiding rehabilitation programs and ensuring patients safety. Falls, as one of the common adverse events in the rehabilitation process of patients with lower limb movement disorders, have a serious impact on the subsequent rehabilitation of patients[30]. Therefore, the fall risk assessment is the first part of the assessment, which is considered as the foundation of fall prevention. Besides, the quantitative and objective walking ability assessment is essential to accurately understand a patient's current level of rehabilitation, which is crucial for making personalized rehabilitation plans[5a]. Furthermore, the fine-grained rehabilitation progress assessment can capture the slight progress made by patients, which is beneficial for enhancing the patient's motivation and adjusting the rehabilitation plans.

Here, we proposed an MG-former model to take advantages of potential relationship between multiple tasks to improve performances on multiple interrelated tasks. **Figure 5**a demonstrates the schematic structure of the MG-former model, which can simultaneously perform multiple tasks including binary classification (Task 1), multiclassification (Task 2), and regression (Task 3). The MG-former model based on self-attention mechanism of transformer can provide rich and robust contextual information when processing sequential data, which is beneficial to accurately capture local or global features in the gait signal and adaptively learn the correlation between different parts[31]. During the data collection process, we employed a 30 Hz low-pass filter using an NI data acquisition card to remove high-frequency noise and interference.

This filtering step is crucial in obtaining high-quality gait signals from the on-skin sensors. The signals with periodicity from on-skin sensors and FSR, which contain diversified information about a dynamic gait cycle, *e.g.*, stride frequency and contacting force between feet and shoes, are cut into a sequence of patches. The size of the patch is closely related to the accuracy of the modelling algorithm, which is set to 100 samples (0.1 seconds × 1000 Hz). Then, the patch sequences are fed into the MG-former model, which consists sequentially of linear projection of patches, position embedding, stacks of transformer encoders, and multitask heads. Each transformer encoder encompasses layer normalization, multi-head self-attention, and multi-layer perceptron (MLP). Finally, the walking ability assessment results are generated from the corresponding task heads. To provide sufficient depth and modelling capability for gait data, the structure of the 8-layer transformer encoder stack was designed. Specifically, each encoder has an 8 attention heads, a forward propagation dimension size of 512, and an MLP with a single layer dimension size of 2048. In addition, the gaussian error linear unit (GELU) was used as the activation function as well as maintaining a dropout rate of 0.1. With each subject, the whole data was divided into the training set (60%) and testing set (40%). The detailed description of the MG-former model is presented in Note S3, Supporting Information.

2.4.1 Task 1: The screening for abnormal gait for fall risk assessment (Stage 1)

Many diseases affect the human body in the form of abnormal gait, leading to increased risk of falls due to balance dysfunction in patients. Therefore, abnormal gait screening can be utilized for fall risk assessment, which is of great significance for physicians to implement early interventions to ensure patient safety. Here, an attending physician from the department of rehabilitation medicine with 10 years of clinical experience in rehabilitation assessment was invited to assess the fall risk of patients

458 according to the conventional Berg Balance Scale (BBS), which served as the golden
459 standard[32]. Specifically, the total score of the BBS is 56 points, with a lower score
460 indicating weaker balance function, and the score less than 40 points indicates the
461 greater risk of falling (Table S2). The results of fall risk assessment from the
462 experienced physician for 15 post-stroke hemiplegic patients (P1-P15, Table S3) in
463 Table S4. Based on the gold standard from the experienced physician, the patients were
464 categorized into two distinct groups: individuals with a lower risk of falling (The score
465 of BBS greater than 40 or equal to 40 points) and those with a higher risk (The score of
466 BBS less than 40 points). Through analyzing the gait data of the patients, the MG-
467 former model enables automated fall risk assessment through binary classification
468 (Task 1). This process identifies the high-risk population promptly, facilitating timely
469 interventions and preventive measures.

470 In order to visualize the overall clustering of the entire gait dataset, we introduced t-
471 distributed stochastic neighbor embedding (t-SNE) in the 2D feature space. The two
472 different colors represent subjects at lower fall risk (light blue) and higher fall risk (rosy
473 red) and each point refers to a sample of gait data projected from the high-dimensional
474 to two dimensions. Figure 5b and c illustrate the t-SNE distributions of subjects with
475 lower and higher fall risk in output layer of the MG-former model before and after
476 training when performing the binary classification task (Task 1). The results
477 demonstrate that there is an optimal feature clustering after training with the MG-former
478 model, in which subjects with higher and lower fall risk display less overlap and strong
479 interclass separability.

480 **2.4.2 Task 2: The objective and quantitative walking ability assessment (Stage 2)**

481 After performing the fall risk assessment, the experienced physician was invited to
482 assess the walking ability of the patient according to the conventional Tinetti scale

(Table S5)[5a].

Firstly, the walking ability of the patients (P1-P15) was assessed by the experienced physician based on the Tinetti scale (0-12 points) as the gold standard (Table S6) for the assessment of the MG-former model. Each point on the Tinetti scale is considered a category in 13 categories, where the higher score represents the better walking ability of the subject. Then, the MG-former model combines the high-quality gait signals captured by the on-skin sensors with the gold standard to achieve quantitative assessment. Specifically, a 13-category classification task (Task 2: multiclassification) based on the MG-former model was also implemented to quantitatively assess the walking ability of 9 healthy subjects and 15 post-stroke hemiplegic patients by supervised learning. Finally, the output category of the model is the prediction score of the corresponding patients.

Since the gait signal is a periodic time-sequence signal, an appropriate sliding window length is crucial for capturing the signal features of the complete gait cycle. At the same time, it can effectively avoid the computational complexity caused by a large sliding window length and the incomplete signal feature capture due to a short sliding window length. Figure 5d demonstrates the effect of different sliding window lengths on the accuracy of gait assessment, which corresponds to a maximum of 96.18% accuracy when the sliding window length is 15 s. As presented in Figure 5e and Figure S12, the results of walking ability assessment by means of the RAP are almost identical to the scores given by the physician based on the conventional Tinetti gait assessment scale, which demonstrates the validity of the RAP. It is worth noting that the results of the walking ability assessment using RAP are presented in the form of mean and standard deviation. This is because each subject's data is divided into multiple samples using a sliding window, as mentioned earlier. Then, these samples are sequentially input

into the MG-former for assessment, and the average value and standard deviation of each subject's assessment results are calculated. A smaller standard deviation indicates lower variability in the assessment results, which implies more reliable outcomes. Figure 5f illustrates the training process of MG-former model, highlighting the changes in accuracy and overall loss function, as well as demonstrating that the neural network can quickly obtain high recognition accuracy and exhibit good stability.

As shown in Figure S14a-e, different types of classification algorithms including CNN, LSTM, fully connected networks (FCN), SVM, and random forest (RF) were used to assess the walking ability of hemiplegic patients with stroke (P1-P15). By comparing the different algorithms, it is found that the accuracy of MG-former model is better than other models (Figure 5g), which indicates that MG-former model shows clear advantages in processing sequential data. This is because the MG-former model is attention mechanism-based and elucidates the nature of the input sequence, dispensing with recurrence and convolutions entirely, thereby allowing input dependencies modeling without regard to distance and enabling the assessment of complex long-range correlations[31]. Meanwhile, the MG-former model enjoys significant parallelizability and global receptive field thanks to self-attention. Therefore, the MG-former model tends to achieve superior performance in large-scale and complex sequential data tasks, especially gait signals. Clinically, hemiplegic gait usually exhibits common characteristics such as decreased step length and gait velocity, as well as increased bilateral asymmetry. However, there are also differences in age, physical condition, and severity that inevitably lead to individual differences in gait of hemiplegic patients. Therefore, it is difficult to build a comprehensive dataset for the gait of hemiplegic patients at one time. Continual learning of the model is an optimum strategy to solve the above problems. The detailed description of the iterative update of

the MG-former model is presented in Note S4, Supporting Information.

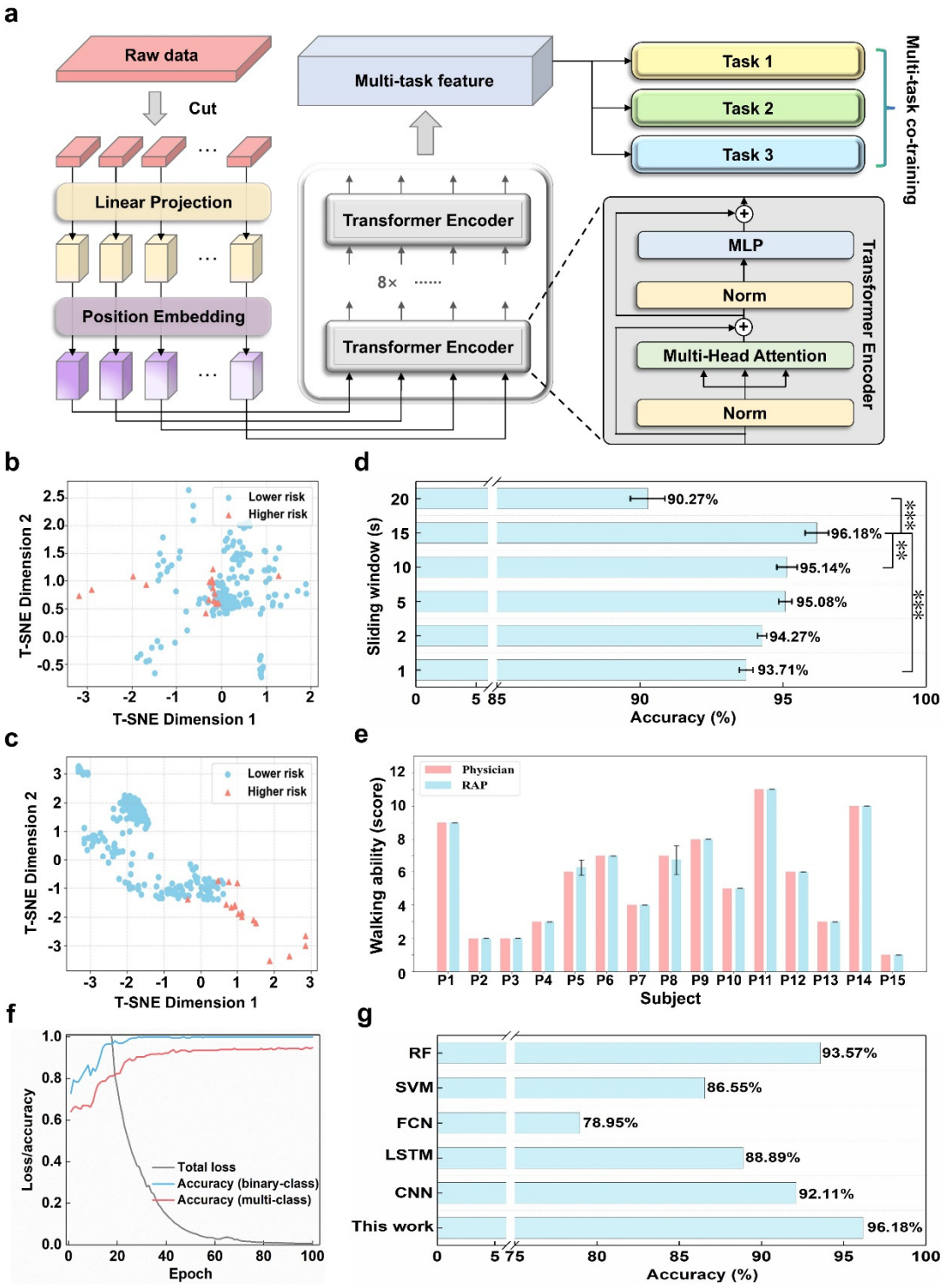

Figure 5. Rehabilitation assessments based on the MG-former model. a) The schematic structure of the MG-former model. b-c) The t-SNE distributions of subjects with higher and lower fall risk in output layer of the MG-former model before and after training when performing the binary classification task. d) The effect of different sliding window lengths on the accuracy of assessment. *p*-Values were calculated using a one-way ANOVA program with Tukey's multiple comparisons post hoc test. (*$p < 0.05$,

541 $^{**}p < 0.01$, $^{***}p < 0.001$, and ns = no significant difference). Data in d) are presented
542 as mean values ± SD, n = 5. e) The comparison of the results of walking ability
543 assessment by an experienced physician and RAP for 15 post-stroke hemiplegic patients
544 (P1-P15). Data in e) are presented as mean values ± SD, n = 3. f) Loss-accuracy curve
545 during model training. g) The comparison of walking ability assessment results based
546 on different types of machine learning model.
547
548 **2.4.3 Task 3: The fine-grained rehabilitation progress assessment (Stage 3)**

549 Rehabilitation progress assessment (**Figure 6**a) plays an essential role in making
550 rehabilitation plans, preventing complications, and assessing progress during the long-
551 term rehabilitation process. However, conventional rehabilitation progress assessment
552 methods struggle to capture these subtle advances, as they usually fall below the
553 minimum precision discernible by such scales. Therefore, in order to further precisely
554 and quantitatively track the progress made by the patients in rehabilitation process, the
555 MG-former model performs the third task (Task 3), i.e. regression prediction (Figure
556 6b). As shown in Figure 6c-i and c-ii, two patients (P_{L1} and P_{L2}, Table S9) with lower
557 limb movement disorders, were invited to perform monitoring for three consecutive
558 weeks. As shown in Figure 6d-f and Movie S3-S5, the $V_{PP\text{-}GM}$ of P_{L1} gradually increased
559 from 0.6 V to 5.11 V after 3 weeks of rehabilitation and the average energy also
560 gradually increased (Figure S18), which indicated that the muscle strength of patient
561 was improved, as well as indirectly proved the effectiveness of the implemented
562 rehabilitation strategy. As presented in Figure S19a, by observing the pressure signals
563 of FSR (V_{FSR}) of P_{L2}, it was found that the patient exhibited an abnormal gait during the
564 walking, characterized by simultaneous elevation and descent of the heel and the toe.
565 Excitingly, the abnormal gait of P_{L2} was recovered after three weeks of rehabilitation
566 training, and the value of FSR2 gradually increased to FSR1, indicating an even
567 distribution of force between the heel and toes during walking (Figure S19a-c and
568 Movie S6-S8). Furthermore, the comparisons of the $V_{PP\text{-}GM}$ of P_{L2} over three weeks
569 reveals a clear increase in the amplitude and the average energy of the triboelectric

signal (Figure S21), suggesting that the level of muscle strength of the patient has been improved. The detailed descriptions of P_{L1} and P_{L2} is presented in Note S5, Supporting Information.

As for the MG-former model, it allows each task to benefit from co-training with other related tasks, which jointly improves the generalization of the model. Thus, the Task 3 can utilize the gait information from Task 1 and Task 2, especially the gait data from the previous 23 patients (P1-P23), to achieve efficient learning under inexact supervision. Specifically, the regression task head of the MG-former model incorporates an additional 8 decoder layers to further capture the slight progress of the patient's rehabilitation process, which includes both time-domain information (Figure 6g and Figure S20) and frequency-domain information (Figure S18 and S21). At the same time, the gait data excluding P_{L1} and P_{L2} were used as the training set and the mean square error of minimizing the assessment scores was taken as the objective function. After training, the MG-former model assessed the walking ability of P_{L1} and P_{L2} based on their multiple sets of sliding window data over three weeks and output a continual value (in the range of 0-12 points) as the result of the walking ability of the patients. The mean of the patient's walking ability assessment results of each week was used as the final result for that week to obtain a more objective assessment. Therefore, the score indicates the walking ability of the patient, where higher score demonstrates better physical recovery. In contrast to the discrete values (integer values in the range of 0-12 points) output from performing the classification task (Task 2), the MG-former model can output continual value (continuous values in the range of 0-12 points) when performing the regression task (Task 3), which can assess the slight progress of patients in the rehabilitation process that cannot be captured by conventional scales. Figure 6h and i display the fine-grained rehabilitation progress assessment results based on MG-

former model within 3 weeks for P_{L1} and P_{L2}, respectively. Clearly, the assessment results of P_{L1} within three weeks were 7.94, 7.89, and 8.42 points respectively, which showed that the rehabilitation progress was not obvious in the first and second weeks, but there was a greater improvement in the third week. For P_{L2}, the walking ability of the patient was steadily improving during the rehabilitation period, gradually increasing from 7.9 to 8.1 points. By capturing the slight progress made by P_{L2} in the rehabilitation process through the RAP, the P_{L2} are encouraged to actively participate in rehabilitation and enhance his self-confidence. Specifically, the V_{FSR2} gradually increased from 0.46 V to 1.41 V close to the V_{FSR1} after 3 weeks of rehabilitation (Figure S19a-c). It is worth noting that, compared with the coarse-grained assessment results of the conventional Tinetti gait assessment scale (integer values in the range of 0-12 points, *e.g.*, 7 or 8 points), the RAP based on the regression task of the MG-former model can capture the slight progress of the patient's rehabilitation process with fine-grained assessment results (continuous values in the range of 0-12 points, *e.g.*, 7.9 or 8.1 points), which is beneficial for adjusting the rehabilitation plans and improving the patient's motivation. Moreover, the fine-grained assessment results provided by RAP can identify potential issues in the rehabilitation process for early intervention and prevention of complications. This is important for patients with lower limb movement disorders, where small improvements can have a significant impact on their overall quality of life. In addition, slight improvement shown by fine-grained assessment results can also improve self-confidence and encourage the patients to be more active to participate in rehabilitation.

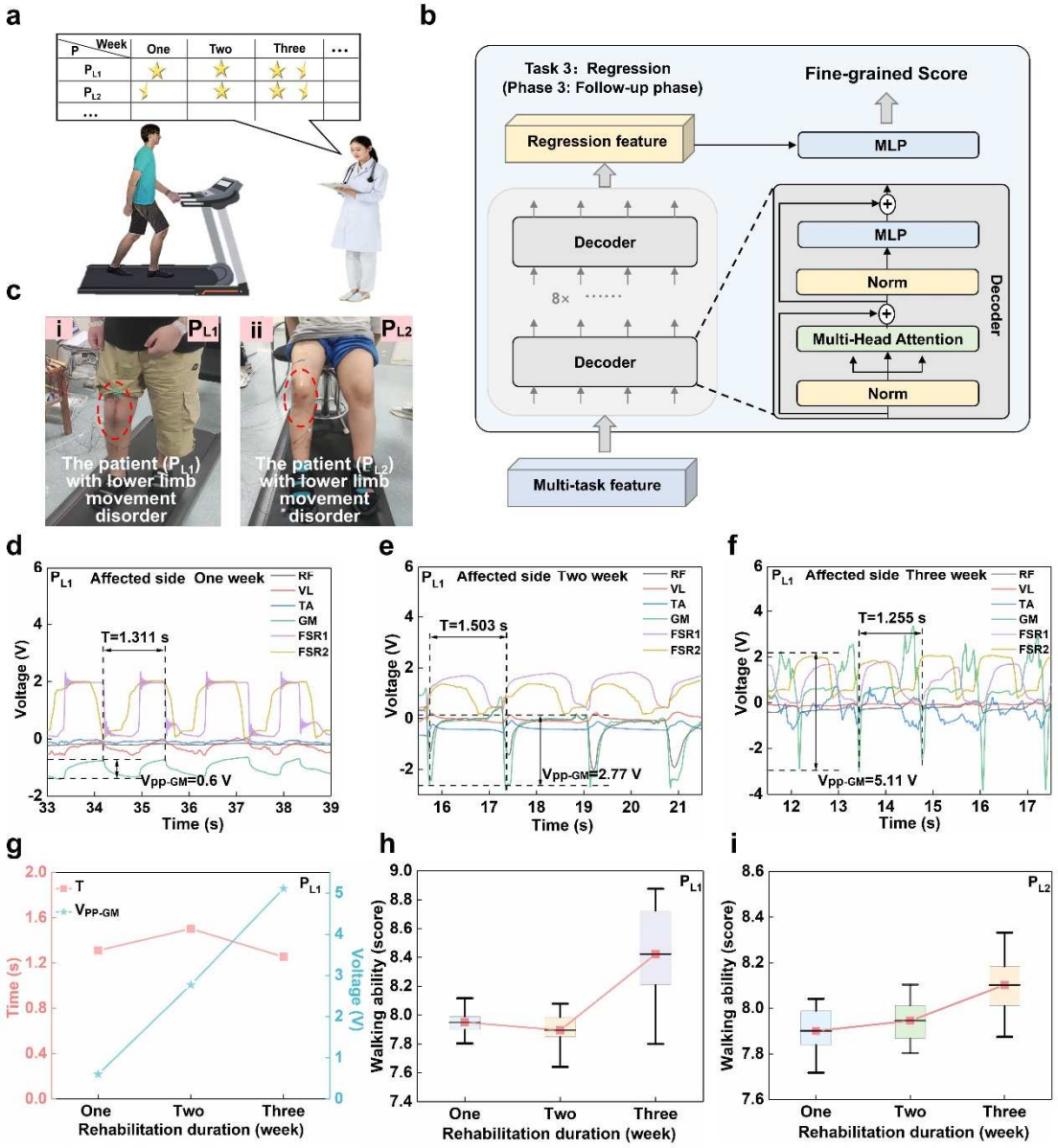

Figure 6. The fine-grained rehabilitation progress assessment based on the MG-former model. a) The diagram of rehabilitation tracking. b) The schematic structure of the MG-former model performs the regression prediction. c-i and c-ii) The photos of patients (P_{L1} and P_{L2}) with lower limb movement disorders. d-f) The complete gait signals on the affected side of P_{L1} for 3 weeks during rehabilitation. g) The evolution of the time intervals (T) and $V_{PP\text{-}GM}$ for P_{L1} with the rehabilitation period. h-i) The rehabilitation progress assessment results of P_{L1} and P_{L2} for three consecutive weeks based on the MG-former model. Data in h) and i) are presented as mean values ± SD, n = 3.

3. Discussion

In summary, we have reported a full-process, fine-grained, and quantitative RAP for patients with lower limb movement disorders, which covers the whole rehabilitation

cycle and realizes an objective and quantitative rehabilitation assessments. Compared with existing methods that can only perform a single-task in one stage of rehabilitation and hardly meet the needs of full-process rehabilitation assessments, this work provides a quantitative and fine-grained approach, which can perform multiple tasks including binary classification, multiclassification, and regression, corresponding to fall risk assessment, walking ability assessment, and rehabilitation progress assessment, respectively, which is beneficial for physicians and patients to implement effective and timely plans throughout the whole rehabilitation process. The flexible and lightweight on-skin sensors allow for direct contact with human skin to enhance the wearing comfort, and the signal quality of on-skin sensor is improved by material and structure design, resulting in a higher SNR compared with commercial sEMG electrodes. By continual learning, the MG-former model achieves an iterative update that allows the RAP to quantitatively assess the walking ability of 23 hemiplegic patients, and the results agree with the scores given by the physician according to the conventional Tinetti gait assessment scale, verifying the accuracy of the method. It is noteworthy that the application of machine learning not only renders the results of rehabilitation assessment more objective and precise, but also saves a considerable amount of labor costs. Furthermore, the RAP based on the regression task of the MG-former model can accurately assess the patient's slight progress in the rehabilitation process with fine-grained assessment results, outperforming the coarse-grained assessment of conventional walking ability assessment scales. The fine-grained rehabilitation progress assessment of patients with the support of RAP was carried out for three weeks, which provided timely feedback to the physicians for developing more effective next step of rehabilitation program.

4. Methods

Fabrication of the on-skin sensor

Firstly, the PDMS (Dow Corning 184) solution was prepared by pouring the curing agent to the base (with a 10:1 mixture of silicone prepolymer and curing agent). The PDMS mixture was supplemented with CCTO nanoparticles at varying weight percentages (0, 4, 8, 12, 16, and 20 wt%) and stirred uniformly for 20 minutes. Secondly, the PDMS/CCTO composite film was fabricated by spinning the coating solution onto an acrylic plate (diameter of 1cm) with a pattern at a spinning rate of 350 rpm for 45 s and then cured at 70 °C for 80 min. The composite film was stripped and the AgNWs solution (Nanjing XFNANO Materials Tech Co., Ltd) sprayed on the surface of the patterned side as the top electrode of the on-skin sensor. After curing the AgNWs, a layer of PDMS was spin-coated on the surface as an encapsulation layer. Then, the PDMS solution was dropped onto an acrylic mold (diameter of 1cm) with circular indentations, followed by placing it in a vacuum and allowing it to settle for 20 minutes to ensure complete filling of the PDMS. The width of the arc-shaped protrusion was fixed at 1 mm. Next, spin-coating was performed at a rate of 350 rpm to ensure a smooth surface of the PDMS and cured in an oven at 70 °C for 60 min. After curing, the prepared ECC was coated on its inner surface as the positive triboelectric layer and the bottom electrode. Finally, the upper and lower layer of the sensor were assembled using PDMS as an adhesive to form the on-skin sensor with a diameter of 1 cm.

Fabrication of the ECC

After being repeatedly washed with anhydrous ethanol, the silver powder was mixed with PDMS matrix in a grinding bowl at a mass ratio of 3:1 and homogenized by grinding for 10 minutes to achieve a uniform mixture.

Characterizations and electrical output measurements

The programmable high-impedance electrometer (Keithley Instruments Model 6514) and a commercial force sensor (Xiamen Enlai Automatic Technology Co. Ltd.) were connected to the USB-6536 data acquisition card (National Instruments) to measure the electrical outputs of the on-skin sensor. The force of 5-25 N was obtained by adjusting the contact separation distance of the linear motor (LinMot, PS01-23 × 80-R). The surface and cross-section morphology of ECC, AgNWs, and CCTO powder were obtained by SEM (Hitachi SU3900). The dielectric properties were measured via a LCR meter (TZDM-RT-1000) over a frequency range of 1 kHz to 300 kHz. The crystallographic structure of the CCTO powder was tested using X-ray diffraction (XRD, Bruker D8 Advance) with Cu Kα radiation (2θ range: 20°–90°). The surface roughness and surface potential of composite film were characterized by KPFM (Park Systems, XE100).

The MG-former model with continual learning

There were three tasks in the MG-former model, and each task had the same input space (input data), which can be expressed as $\boldsymbol{X} = \{\boldsymbol{x}_j\}_{j=1}^{n}$, where n represented the number of samples. The output space (predicted values) for each task varies, denoted as $\boldsymbol{Y}_i = \{y_{i,j}\}_{j=1}^{n}, i = 1,2,3$. The learning goal of MG-former model was to find the optimal functions f_i to minimize the following cumulative multitask loss:

$$\mathcal{L} = \sum_{i=1}^{3}\sum_{j=1}^{n} \alpha_i \mathcal{L}_i\left(f_i(\boldsymbol{x}_j), y_{i,j}\right) \quad (2)$$

where $\mathcal{L}_i\left(f_i(\boldsymbol{x}_j), y_{i,j}\right) \triangleq \mathcal{C}_i\left(f_i(\boldsymbol{x}_j), y_{i,j}\right) + \lambda_i\|f_i\|^2$, $\mathcal{C}_i$ was a cost function for task i, $\|f_i\|^2$ was the regularization term with parameter λ_i to control overfitting. The α_i were the trade-off parameters among tasks.

When new data $\boldsymbol{X}' = \{\boldsymbol{x}_j'\}_{j=1}^{n'}$, $\boldsymbol{Y}_i' = \{y_{i,j}'\}_{j=1}^{n'}$ was collected, a knowledge distillation method based on teacher-student framework was introduced into the MG-

former model.

The cumulative loss of the student model on the new data was as follows:

$$\mathcal{L}' = \sum_{i=1}^{3} \sum_{j=1}^{n'} \alpha_i \mathcal{L}_i\left(f_i'\left(\boldsymbol{x}_j'\right), y_{i,j}'\right) \quad (3)$$

However, direct minimization causes the student model to forget the old knowledge. Therefore, the teacher model was still needed to guide the learning process by minimizing the distillation loss:

$$\mathcal{L}_{distillation} = \frac{1}{n'} \sum_{j=1}^{n'} d\left(\boldsymbol{z}_i'\left(\boldsymbol{x}_j'\right), \boldsymbol{z}_i\left(\boldsymbol{x}_j'\right)\right) \quad (4)$$

where $\boldsymbol{z}_i(\boldsymbol{x})$ and $\boldsymbol{z}_i'(\boldsymbol{x})$ donate the output layer representations of the teacher model and student model at input $\boldsymbol{x}$, respectively. The function $d(\cdot,\cdot)$ computes the similarity between two representations, which was defined as the Euclidean distance in this paper. Then, the overall loss of the student model was defined as:

$$\mathcal{L}_{student} = \beta_1 \mathcal{L}' + \beta_2 \mathcal{L}_{distillation} \quad (5)$$

where β_1 and β_2 were trade-off parameters that control the balance between multi-task cumulative loss and distillation loss. The detailed description was presented in Note S4, supporting information.

Ethics Oversight

All procedures in the tests in healthy individuals and patients were in accordance with the experimental protocol approved by the Medical Ethics Committee, Union Hospital, Tongji Medical College, Huazhong University of Science and Technology (UHCT-IEC-SOP-016-03-01). All subjects agreed with the study procedures and provided signed consent forms.

Statistical Analysis

All data were processed and analyzed in Microsoft Excel, MATLAB (MathWorks), and Origin. All data were presented as the mean ± the standard deviation (SD) with at least 3 samples unless reported elsewise. Statistical significance of the variance was

evaluated by the GraphPad prism (Version 7.0) using the one-way analysis of variance (ANOVA) program with Tukey's multiple comparisons post hoc test. Values of *p<0.05, **p<0.01 and ***p<0.001 were considered statistically significant. And "ns" mean no significant difference.

Supplementary Materials

Note S1 to S5
Figure S1 to S21
Tables S1 to S10
Movies S1 to S8

Conflict of interest

The authors declare no conflict of interest.

Author Contributions

Z.X.W. and X.R.H. contributed equally to this work. H.W., Z.P.Y., J.H., Z.X.W., and X.R.H. conceived the concept and designed the experiments. Z.X.W. conducted on-skin sensor fabrication and data analysis. X.L.X., Z.X.W., X.R.H., B.P., Z.Y.T., and W.G. implemented the tests on clinical cases. Z.X.W. and X.R.H. wrote the manuscript with contributions from all authors. H.W., J.H., Z.Q.Z., T.Z.B, and Z.P.Y. revised the original draft. All authors discussed the results and approved the final version of the paper.

Data availability

The data that support the findings of this study are available from the corresponding author upon reasonable request.

Acknowledgments

We acknowledge the support from National Natural Science Foundation of China (No. 52350121, U2013213, 92048302, and 52188102), the Fundamental Research Funds for the Central Universities (HUST: 2024JYCXJJ030 and YCJJ20230217), and the STAR Project by the School of Mechanical Science and Engineering of Huazhong University of Science and Technology. We also acknowledge the support from Flexible Electronics Research Center of HUST for providing experiment facility. We thank to the Analytical & Testing Centre of Huazhong University of Science and Technology for providing support in the characterization of composite film. We thank engineers Wei Xu, and Guangxue Zhang in the Center of Optoelectronic Micro&Nano Fabrication and Characterizing Facility, Wuhan National Laboratory for Optoelectronics of Huazhong University of Science and Technology for the support in device measurement (XRD test). This work was supported by the Taihu Lake Innovation Fund for Future Technology, HUST (2023A3).

References

[1] a) T. Foltynie, *Cell Stem Cell* **2024**, 31, 5; b) K. B. Baker, E. B. Plow, S. Nagel, A. B. Rosenfeldt, R. Gopalakrishnan, C. Clark, A. Wyant, M. Schroedel, J. Ozinga, S. Davidson, O. Hogue, D. Floden, J. Chen, P. J. Ford, L. Sankary, X. Huang, D. A. Cunningham, F. P. DiFilippo, B. Hu, S. E. Jones, F. Bethoux, S. L. Wolf, J. Chae, A. G. Machado, *Nature Medicine* **2023**, 29, 2366.

[2] a) P. Boyne, S. A. Billinger, D. S. Reisman, O. O. Awosika, S. Buckley, J. Burson, D. Carl, M. DeLange, S. Doren, M. Earnest, M. Gerson, M. Henry, A. Horning, J. C. Khoury, B. Kissela, A. Laughlin, K. McCartney, T. McQuaid, A. Miller, A. Moores, J. A. Palmer, H. Sucharew, E. D. Thompson, E. Wagner, J. Ward, E. P. Wasik, A. A. Whitaker, H. Wright, K. Dunning, *Jama Neurology* **2023**, 80, 342; b) L. Tang, Y. Yin, H. Liu, M. Zhu, Y. Cao, J. Feng, C. Fu, Z. Li, W. Shu, J. Gao, X. J. Liang, W. Wang, *Advanced Materials* **2024**, 36, 2312897.

[3] P. Slade, M. J. Kochenderfer, S. L. Delp, S. H. Collins, *Nature* **2022**, 610, 277.

[4] C. Li, H. Yang, L. Cheng, F. Huang, S. Zhao, D. Li, R. Yan, *IEEE Transactions on Neural Systems and Rehabilitation Engineering* **2022**, 30, 2032.

[5] a) Q. Yan, J. Huang, D. Wu, Z. Yang, Y. Wang, Y. Hasegawa, T. Fukuda, *IEEE Transactions on Neural Systems and Rehabilitation Engineering* **2022**, 30, 2916; b) M. Penta, L. Tesio, C. Arnould, A. Zancan, J. L. Thonnard, *Stroke* **2001**, 32, 1627.

[6] S. Zhang, L. Fan, J. Ye, G. Chen, C. Fu, Y. Leng, *IEEE Transactions on Neural Systems and Rehabilitation Engineering* **2023**, 31, 3106.

[7] a) H. Wu, Z. Li, Z. Xu, X. Huang, W. Guo, J. Zhao, J. W. Zhang, S. Y. Liu, M. Tang, Y. Q. Qiu, G. G. Yang, J. T. Zhu, L. L. Liu, Y. J. Wu, W. Lei, P. Zhou, Z. P. Yin, Z. B. Chen, Y. T. Liu, *Science Translational Medicine* **2023**, 15, eabq1634; b) G. Yang, Y. Hu, W. Guo, W. Lei, W. Liu, G. Guo, C. Geng, Y. Liu, H. Wu, *Advanced Materials* **2023**, 23, 2308831; c) Q. Yang, W. Jin, Q. Zhang, Y. Wei, Z. Guo, X. Li, Y. Yang, Q. Luo, H. Tian, T.-L. Ren, *Nature Machine Intelligence* **2023**, 5, 169; d) D. Wei, J. Guo, Y. Qiu, S. Liu, J. Mao, Y. Liu, Z. Chen, H. Wu, Z. Yin, *National Science Review* **2022**, 9, nwac227; e) J. Engelmann, A. D. McTrusty, I. J. C. MacCormick, E. Pead, A. Storkey, M. O. Bernabeu, *Nature Machine Intelligence* **2022**, 4, 1143; f) X. Huang, W. Guo, S. Liu, Y. Li, Y. Qiu, H. Fang, G. Yang, K. Zhu, Z. Yin, Z. Li, H. Wu, *Advanced Functional Materials* **2022**, 32, 2109109; g) S. Jin, H. Choi, D. Seong, C.-L. You, J.-S. Kang, S. Rho, W. B. Lee, D. Son, M. Shin, *Nature* **2023**, 623, 58; h) F. B. Wagner, J.-B. Mignardot, C. G. Le Goff-Mignardot, R. Demesmaeker, S. Komi, M. Capogrosso, A. Rowald, I. Seáñez, M. Caban, E. Pirondini, M. Vat, L. A. McCracken, R. Heimgartner, I. Fodor, A. Watrin, P. Seguin, E. Paoles, K. Van Den Keybus, G. Eberle, B. Schurch, E. Pralong, F. Becce, J. Prior, N. Buse, R. Buschman, E. Neufeld, N. Kuster, S. Carda, J. von Zitzewitz, V. Delattre, T. Denison, H. Lambert, K. Minassian, J. Bloch, G. Courtine, *Nature* **2018**, 563, 65.

[8] T. v. Marcard, G. Pons-Moll, B. Rosenhahn, *IEEE Transactions on Pattern Analysis and Machine Intelligence* **2016**, 38, 1533.

[9] a) O. Dehzangi, M. Taherisadr, R. ChangalVala, *Sensors* **2017**, 17, 2735; b) J. A. Ramirez-Bautista, J. A. Huerta-Ruelas, S. L. Chaparro-Cardenas, A. Hernandez-Zavala, *IEEE Reviews in Biomedical Engineering* **2017**, 10, 299.
[10] a) Q. Shi, Z. Zhang, T. He, Z. Sun, B. Wang, Y. Feng, X. Shan, B. Salam, C. Lee, *Nature Communications* **2020**, 11, 4609; b) J. L. Chen, Y. N. Dai, N. S. Grimaldi, J. J. Lin, B. Y. Hu, Y. F. Wu, S. Gao, *Advanced Materials Technologies* **2021**, 7, 2100566.
[11] a) Y. Song, R. Y. Tay, J. Li, C. Xu, J. Min, E. S. Sani, G. Kim, W. Heng, I. Kim, W. Gao, *Science Advances* **2023**, 13, eadi6492; b) J. P. Lee, H. Jang, Y. Jang, H. Song, S. Lee, P. S. Lee, J. Kim, *Nature Communications* **2024**, 15, 530.
[12] G. Yang, K. Zhu, W. Guo, D. Wu, X. Quan, X. Huang, S. Liu, Y. Li, H. Fang, Y. Qiu, Q. Zheng, M. Zhu, J. Huang, Z. Zeng, Z. Yin, H. Wu, *Advanced Functional Materials* **2022**, 32, 2200457.
[13] H. Fang, L. Wang, Z. Fu, L. Xu, W. Guo, J. Huang, Z. L. Wang, H. Wu, *Advanced Science* **2023**, 10, 2205960.
[14] L. Shi, V. S. Kale, Z. Tian, X. Xu, Y. Lei, S. Kandambeth, Y. Wang, P. T. Parvatkar, O. Shekhah, M. Eddaoudi, H. N. Alshareef, *Advanced Functional Materials* **2023**, 33, 2212891.
[15] Y. Li, Y. Luo, H. Deng, S. Shi, S. Tian, H. Wu, J. Tang, C. Zhang, X. Zhang, J. W. Zha, S. Xiao, *Advanced Materials* **2024**, 20, 2314380.
[16] C. Cui, G.-B. Bian, Z.-G. Hou, J. Zhao, G. Su, H. Zhou, L. Peng, W. Wang, *IEEE Transactions on Neural Systems and Rehabilitation Engineering* **2018**, 26, 856.
[17] Z. Zhang, T. He, M. Zhu, Z. Sun, Q. Shi, J. Zhu, B. Dong, M. R. Yuce, C. Lee, *npj Flexible Electronics* **2020**, 4, s41528.
[18] C. Estrada-Barranco, I. Sanz-Esteban, M. J. Giménez-Mestre, R. Cano-de-la-Cuerda, F. Molina-Rueda, *Journal of Clinical Medicine* **2022**, 11, 3771.
[19] W. Guo, P. Zheng, X. Huang, H. Zhuo, Y. Wu, Z. Yin, Z. Li, H. Wu, *ACS Applied Materials & Interfaces* **2019**, 11, 8567.
[20] Y. Song, M. Liu, J. Bao, Y. Hu, M. Xu, Z. Yang, Q. Yang, H. Cai, C. Xiong, Z. Shi, *Carbohydrate Polymers* **2022**, 298, 120111.
[21] a) Y. Lu, Q. H. Qin, J. J. Meng, Y. J. Mi, X. Q. Wang, X. Cao, N. Wang, *Chemical Engineering Journal* **2023**, 468, 143802; b) J. Chen, H. Guo, X. He, G. Liu, Y. Xi, H. Shi, C. Hu, *ACS Applied Materials & Interfaces* **2015**, 8, 736; c) J. Kim, H. Ryu, J. H. Lee, U. Khan, S. S. Kwak, H. J. Yoon, S. W. Kim, *Advanced Energy Materials* **2020**, 10, 1903524; d) C. Cai, T. Chen, X. Chen, Y. t. Zhang, X. h. Gong, C. g. Wu, T. Hu, *Macromolecular Materials and Engineering* **2021**, 306, 2100046; e) P. Manchi, S. A. Graham, M. V. Paranjape, A. Kurakula, V. S. Kavarthapu, J. S. Yu, *Journal of Materials Science & Technology* **2024**, 190, 56.
[22] a) B. Xi, L. Wang, B. Yang, Y. Xia, D. Chen, X. Wang, *Nano Energy* **2023**, 110, 108385; b) H. Kang, H. T. Kim, H. J. Woo, H. Kim, D. H. Kim, S. Lee, S. Kim, Y. J. Song, S.-W. Kim, J. H. Cho, *Nano Energy* **2019**, 58, 227.
[23] a) Z. Wang, Y. Wu, W. Jiang, Q. Liu, X. Wang, J. Zhang, Z. Zhou, H. Zheng, Z. Wang, Z. L. Wang, *Advanced Functional Materials* **2021**, 31, 2103081; b) X.

Huang, T. Bu, Q. Zheng, S. Liu, Y. Li, H. Fang, Y. Qiu, B. Xie, Z. Yin, H. Wu, *National Science Review* **2024**, 11, nwae027.
[24] D. Liu, D. Zhang, Z. Sun, S. Zhou, W. Li, C. Li, W. Li, W. Tang, Z. L. Wang, *Advanced Functional Materials* **2022**, 32, 2113008.
[25] X. Shi, P. Qin, J. Zhu, M. Zhai, W. Shi, *IEEE Access* **2020**, 8, 132882.
[26] a) L. Nguyen, L.-C. Xu, E. Yeager, W. J. Weiss, C. A. Siedlecki, *Journal of Biomaterials Applications* **2023**, 38, 302; b) A. T. Stevenson, L. M. Reese, T. K. Hill, J. McGuire, A. M. Mohs, R. Shekhar, L. R. Bickford, A. R. Whittington, *Biomaterials* **2015**, 54, 168.
[27] M. Ye, C. Yang, V. Stankovic, L. Stankovic, S. Cheng, *IEEE Transactions on Multimedia* **2020**, 22, 1113.
[28] C. W. Tsao, A. W. Aday, Z. I. Almarzooq, A. Alonso, A. Z. Beaton, M. S. Bittencourt, A. K. Boehme, A. E. Buxton, A. P. Carson, Y. Commodore-Mensah, M. S. V. Elkind, K. R. Evenson, C. Eze-Nliam, J. F. Ferguson, G. Generoso, J. E. Ho, R. Kalani, S. S. Khan, B. M. Kissela, K. L. Knutson, D. A. Levine, T. T. Lewis, J. Liu, M. S. Loop, J. Ma, M. E. Mussolino, S. D. Navaneethan, A. M. Perak, R. Poudel, M. Rezk-Hanna, G. A. Roth, E. B. Schroeder, S. H. Shah, E. L. Thacker, L. B. VanWagner, S. S. Virani, J. H. Voecks, N.-Y. Wang, K. Yaffe, S. S. Martin, *Circulation* **2022**, 145, e153.
[29] G. Yavuzer, F. Eser, D. Karakus, B. Karaoglan, H. J. Stam, *Clinical Rehabilitation* **2016**, 20, 960.
[30] B.-B. Koo, P. Bergethon, W. Q. Qiu, T. Scott, M. Hussain, I. Rosenberg, L. R. Caplan, R. A. Bhadelia, *Archives of Neurology* **2012**, 69, 733.
[31] S. A. Khan, A. Maillo, V. Lagani, R. Lehmann, N. A. Kiani, D. Gomez-Cabrero, J. Tegner, *Nature Machine Intelligence* **2023**, 5, 1437.
[32] S. Downs, J. Marquez, P. Chiarelli, *Journal of Physiotherapy* **2014**, 60, 85.